

Modeling of diffuse auroral emission at Mars: Contribution of MeV protons

Yuki Nakamura, Naoki Terada, François Leblanc, Ali Rahmati, Hiromu Nakagawa, Shotaro Sakai, Sayano Hiruba, Ryuho Kataoka, Kiyoka Murase

▶ **To cite this version:**

Yuki Nakamura, Naoki Terada, François Leblanc, Ali Rahmati, Hiromu Nakagawa, et al.. Modeling of diffuse auroral emission at Mars: Contribution of MeV protons. Journal of Geophysical Research Space Physics, 2022, 127 (1), pp.e2021JA029914. 10.1029/2021JA029914 . insu-03517910

HAL Id: insu-03517910
https://insu.hal.science/insu-03517910

Submitted on 10 Jan 2022

HAL is a multi-disciplinary open access archive for the deposit and dissemination of scientific research documents, whether they are published or not. The documents may come from teaching and research institutions in France or abroad, or from public or private research centers.

L'archive ouverte pluridisciplinaire **HAL**, est destinée au dépôt et à la diffusion de documents scientifiques de niveau recherche, publiés ou non, émanant des établissements d'enseignement et de recherche français ou étrangers, des laboratoires publics ou privés.

Modeling of diffuse auroral emission at Mars: Contribution of MeV protons

Yuki Nakamura[1,2], Naoki Terada[1], Francois Leblanc[2], Ali Rahmati[3], Hiromu Nakagawa[1], Shotaro Sakai[1,4], Sayano Hiruba[1], Ryuho Kataoka[5,6], and Kiyoka Murase[5,6]

[1]Graduate School of Science, Tohoku University, Sendai, Japan
[2]LATMOS/CNRS, Sorbonne Université, Paris, France
[3]Space Sciences Laboratory, University of California, Berkeley, CA, USA
[4]Planetary Plasma and Atmospheric Research Center, Graduate School of Science, Tohoku University, Sendai, Japan
[5]National Institute of Polar Research, Tokyo, Japan
[6]The Graduate University for Advanced Studies, SOKENDAI, Kanagawa, Japan

Corresponding author: Yuki Nakamura (yuki.nakamura.r2@dc.tohoku.ac.jp)

Key Points:

- A Monte Carlo model was developed to investigate the contributions of precipitating electrons and protons to the diffuse auroral emission.
- Proton-induced CO_2^+ UVD emissions have lower peak altitudes than electron-induced emissions.
- The MAVEN/IUVS limb emission profiles of CO_2^+ UVD during two SEP events were reproduced by considering the contribution of SEP protons.

Abstract (236 words/ up to 250 words)

The Solar Energetic Particle and Imaging UltraViolet Spectrograph (IUVS) instruments onboard the Mars Atmosphere and Volatile EvolutioN (MAVEN) spacecraft discovered diffuse aurora that span across the nightside of Mars due to the interaction of solar energetic particles (SEPs) with the Martian atmosphere. However, it is unclear whether the diffuse aurora originates from energetic electrons or protons. We have developed a Monte Carlo model to calculate the limb intensity profile of the CO_2^+ ultraviolet doublet (UVD) due to precipitation of energetic electrons and protons with energy ranges from 100 eV to 100 keV and from 50 keV to 5 MeV, respectively. We used electron and proton fluxes observed by MAVEN during the December 2014 SEP event and the September 2017 SEP event. Our results showed that proton-induced CO_2^+ UVD emission has a lower peak altitude than electron-induced CO_2^+ UVD emission. The calculated peak altitudes of the CO_2^+ UVD limb profiles are 76 km and 68 km in the December 2014 event and the September 2017 event, respectively. Extending the energy to 500 keV for electrons and 20 MeV for protons further improved our comparison to the IUVS observations. We have succeeded in reproducing peak altitudes and shapes of the observed CO_2^+ UVD limb profiles using the SEP flux observed by MAVEN. This was possible by taking into account the contribution of energetic protons, indicating that both energetic electrons and protons contribute to producing the observed diffuse aurora.

1. Introduction

Solar energetic particles (SEPs) can easily penetrate deep into the atmosphere owing to insufficient magnetospheric and atmospheric shielding of Mars (Leblanc et al., 2002). Penetration of SEPs into the Martian atmosphere leads to increased ionization, heating of the atmosphere and alteration of the atmospheric chemistry (Leblanc et al., 2002; Jolitz et al. 2017; Haider and Masoom, 2019; Gérard et al., 2017; Lingam et al., 2018). One of the consequences of the interaction of SEPs with the Martian atmosphere is the production of auroral emissions (Schneider et al., 2015).

There are three types of aurora that have been identified on Mars: discrete aurora, proton aurora, and diffuse aurora. The discrete aurora was first detected by the Mars Express in the crustal magnetic field region (Bertaux et al., 2005) and is believed to be caused by the acceleration of electrons due to the electric potential along open magnetic field lines (Brain et al., 2006). The discrete aurora is characterized by a strongly localized patch-like

morphology of the emissions and a peak altitude of approximately 120 km, which indicates that precipitation of a few keV electrons causes the discrete aurora (e.g., Bertaux et al., 2005). The proton aurora was first detected by the Mars Atmosphere and Volatile EvolutioN (MAVEN) spacecraft on the dayside of Mars (Deighan et al., 2018; Ritter et al., 2018). Proton aurorae are produced by solar wind protons that are neutralized by charge exchange with exospheric hydrogen atoms outside the Mars' induced magnetosphere. They travel without losing energy up to the atmosphere, where they collide with Mars' main atmospheric constituent, CO_2, become excited and produce Lyman-α emissions. These proton aurorae are visible preferentially during the dayside southern summer solstice (near the solar longitude (Ls), which is 270° when the Mars hydrogen exosphere is the densest) and display a brightness profile peaking at an altitude of approximately 120 km (Hughes et al., 2019).

Recently, MAVEN discovered a new type of aurora, namely, diffuse aurora, that spans the Mars nightside and results from the interaction of SEPs with the Martian atmosphere (Schneider et al., 2015, 2018). This new type of diffuse aurora on Mars is characterized by global brightening and by its low peak altitude of ~60 km, which indicates that more energy is deposited deep in the Martian atmosphere than previously observed. Previous models suggested that 100 keV of monoenergetic electron precipitation should have been at the origin of the low altitude (~60 km) peak of the limb emission; however, no model was able to reproduce the observed emission profiles by using the observed energetic electron flux (Schneider et al., 2015; Gérard et al., 2017; Haider and Masoom, 2019). Previous auroral emission models did not take into account the contribution of MeV proton precipitation, although MeV protons can penetrate down to ~70 km altitude as well (Jolitz et al., 2017). Observations of SEP electron and ion fluxes with the Solar Energetic Particle instrument during the aurorae observed by Imaging UltraViolet Spectrograph (IUVS) instruments onboard MAVEN suggested that both electron and proton energetic populations could have been at the origin of the diffuse aurora (Schneider et al., 2018).

We have developed a Monte Carlo model of Particle TRansport In Planetary atmospheres (PTRIP). PTRIP describes the motion of electrons, protons and hydrogen atoms in the Martian atmosphere. We calculated the limb intensity profile of the CO_2^+ ultraviolet doublet (UVD) due to precipitating electrons and protons with energies ranging from 100 eV - 100 keV and 50 keV - 5 MeV, respectively, as observed by MAVEN during the December 2014 SEP event and September 2017 SEP event.

2. Model Description

PTRIP is a Monte Carlo model that is designed to examine the transport and collisions of electrons, protons and hydrogen atoms that precipitate into the Martian atmosphere. The key assumptions in this study are as follows: (1) we ignore the effects of the electric and magnetic fields on the particle trajectory, (2) atmospheric particles are at rest with respect to incident particles, (3) each incident particle is independent and does not collide or interact with other incident particles, and (4) initial incident angles with respect to the atmosphere are isotropically distributed over one hemisphere directed vertically downward. PTRIP solves the three velocity components of the particle but takes into account only the trajectory of the particle along the altitude. Incident particles are traced below an altitude of 500 km. This study focuses on the emission rate of CO_2^+ UVD with an ionizing threshold energy of ~18 eV, so particles below 15 eV are suppressed from the simulation.

2.1 Monte Carlo Transport Model

In PTRIP, a random number is used to determine whether there is a collision at each time step for each incident particle. The collision probability P_c for a particle traveling along a distance Δl is expressed as:

$$P_c = 1 - \exp\left[-\sum_s n_s(\boldsymbol{l})\, \sigma_s^T(E)\, \Delta l\right] \qquad (1)$$

where $n_s(\boldsymbol{l})$ is the number density of the sth atmospheric species at particle location $\boldsymbol{l}$, $\sigma_s^T(E)$ is the total collisional cross section of the sth atmospheric species for particle energy E, and $\Delta l = |v\Delta t|$, where v is the absolute velocity of the particle and Δt is the time step. A collision occurs if a random number determined from a uniform distribution in a range [0, 1] is less than P_c. Since P_c is the sum of the probabilities for n collisions during Δt (n = 1, 2, 3, …), the accuracy of the collision probability depends on Δt. Δt is determined so that the number of collisions not taken into account during Δt is less than 0.01, which requires P_c to be less than 0.1 (Vahedi and Surrendra, 1995). If a collision occurs, another random number is used to determine the type of collision so that the probability of each type of collision is weighted by the ratio of the frequency of each type of collision to the total collision frequency (Vahedi and Surrendra, 1995).

Several inputs are required by PTRIP. Regarding the incident particles, we need to define the initial type (electron or proton), the initial energy and the number of incident particles. The initial energy of electrons is a set of 16 logarithmically spaced energy bins in a range [100 eV - 100 keV], and the initial energy of protons is a set of 11 logarithmically spaced energy bins in a range [50 keV - 5 MeV]. The number of incident particles at each incident energy is selected to be 1000. Regarding the atmospheric species and their interactions with the incident particles, we defined the atmospheric neutral density profiles, the inelastic and elastic cross sections, energy loss, scattering angle distributions, and the produced secondary electron energy. In this study, we use the atmospheric density profiles for the 5 main species (CO_2, CO, N_2, O_2 and O) from the nightside of the northern hemisphere as calculated by the Mars Climate Database (MCD) version 5.3 (Millour et al., 2018). CO_2 is the most important constituent in this study because we focus on the ionization of CO_2 to generate CO_2^+ UVD emissions. Figure 1 shows atmospheric neutral density profiles used in this study for the December 2014 SEP event and September 2017 SEP event. The solar longitude (Ls) was 255° (near perihelion) on 20 December 2014 and 60° (near aphelion) on 13 September 2017, corresponding to the season of atmospheric inflation and contraction on Mars, respectively (e.g., Forget et al., 2009). The solar activity and the dust load are set to be average. The latitude and local time are set to be 35°N, 00:00, respectively, to match the IUVS observation geometry when the diffuse aurora profile was obtained (Schneider et al., 2015). The CO_2 number density at an altitude of 80 km was 8.5×10^{19} m^{-3} on 20 December 2014 and 3.1×10^{19} m^{-3} on 13 September 2017. Other inputs regarding the interactions of incident particles with atmospheric species are explained in the following sections.

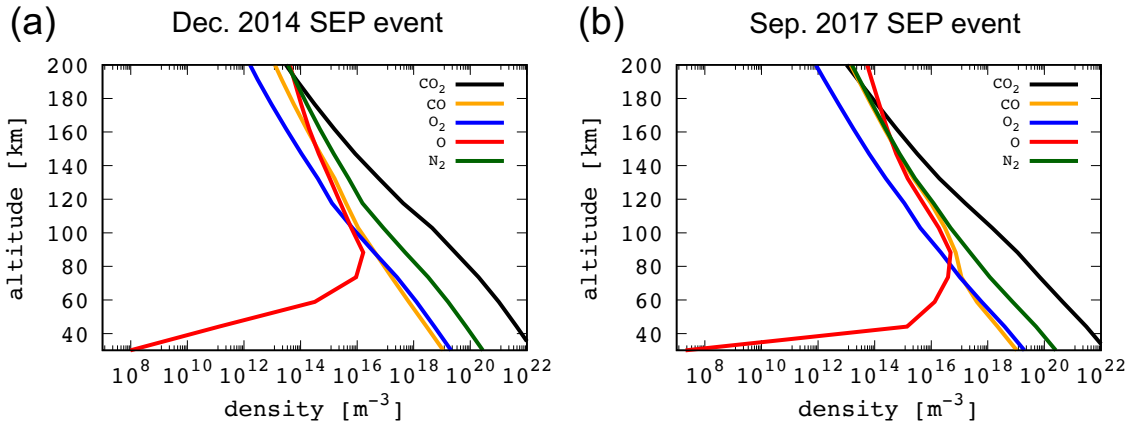


Figure 1(a) Atmospheric density profile on 20 December 2014 and (b) atmospheric density profile on 13 September 2017 used in the Monte Carlo simulations. These density profiles were calculated by the Mars

Climate Database.

2.2 Collisional Cross Sections

PTRIP takes into account elastic and inelastic cross sections of impacting electrons, protons and hydrogen atoms with atmospheric species. First, we describe the elastic and inelastic cross sections due to electron impacts. We calculate the total elastic cross sections of CO_2, CO, N_2, O_2 and O by the formula of Yalcin et al. (2006), which is applicable to 1 keV - 1 MeV. Below 1 keV, we use the total elastic cross section of CO_2 recommended by Itikawa (2002), of CO recommended by Itikawa (2015), of N_2 recommended by Itikawa (2006), of O_2 recommended by Itikawa (2009) and of O in Porter et al. (1978, 1987). The analytic fits of differential ionization cross sections of CO_2 are taken from Bhardwaj and Jain (2009), including the production of 4 excited states ($X^2\Pi_g$, $A^2\Pi_u$, $B^2\Sigma_u^+$, and $C^2\Sigma_g^+$), dissociative ionization, and double ionization. The analytic fits of the differential ionization cross sections of N_2, O_2 and O are taken from Jackman et al. (1977). The accuracy of the energetic electron transport model depends on the accuracy of the ionization cross section of CO_2 because energetic electrons lose energy mostly by ionizing collisions with CO_2. The total ionization cross section of CO_2 used in this study was ~3.0×10^{-22} m^2 at 100 keV, which agrees well with the observed value of ~3.2×10^{-22} m^2 at 100 keV by Rieke and Prepejchal (1972). The analytic fits of differential excitation cross sections of CO_2 are taken from Bhardwaj and Jain (2009). For the fundamental three vibrational excitations of CO_2, (010), (100), and (001), within the energy range of 1.5 eV to 30 eV are taken from Itikawa (2002).

Second, we describe the elastic and inelastic cross sections due to proton impacts. The differential screened Rutherford cross section for the elastic scattering of protons by atoms without correction for relativistic effects can be expressed as:

$$\frac{d\sigma}{d\Omega}(E,\theta) = \left(\frac{Ze}{8\pi\varepsilon_0 E}\right)^2 \frac{1}{(1-\cos\theta+2\eta)^2} \qquad (2)$$

where Ω is the solid angle, Z is the atomic number of the target particle, e is the elementary charge, ε_0 is the permittivity in space, E is the incident proton energy in units of eV, θ is the scattering angle, and η is the screening parameter. The screening parameter η is expressed as (Nigam et al., 1959):

$$\eta = \frac{1}{4}\left(1.12\frac{\lambda}{2\pi a}\right)^2 \qquad (3)$$

where λ is the de Broglie wavelength ($\lambda = h/p$, h is the Planck constant and p is momentum of a proton) and a is the Fermi radius of the atom ($a = 0.885 a_0 Z^{-1/3}$, a_0

is the Bohr radius a_0 = 5.29×10^{-11} [m]). The total elastic cross section can be expressed by integrating equation (2) over the solid angle Ω:

$$\sigma(E) = \left(\frac{Ze}{8\pi\varepsilon_0 E}\right)^2 \frac{\pi}{\eta(1+\eta)} \qquad (4)$$

For the study of proton transport in a planetary atmosphere, the differential and total elastic cross sections from Kallio and Barabash (2001) have been widely used in many models (e.g., Fang et al., 2013; Jolitz et al., 2017) and are based on the observation of hydrogen atom-impact elastic cross sections up to 5 keV (Newman et al., 1986; Noël and Prölss, 1993). The observed differential elastic cross section of 5.34 MeV proton impacts on carbon atoms at a scattering angle of 60 degrees is 3.2×10^{-30} m^2 (Shute et al., 1962); however, the differential elastic cross section from Kallio and Barabash (2001) for incident 5.34 MeV proton at a scattering angle of 60 degrees is 8.2×10^{-27} m^2, which is calculated by the formula described in Kallio and Barabash (2001); this value is 3 orders of magnitude larger than the observed value reported by Shute et al. (1962). The differential elastic cross section of carbon for an incident 5.34 MeV proton at the scattering angle of 60 degrees calculated by equation (2) is 2.6×10^{-30} m^2, which is in good agreement with the observed differential elastic cross section from Shute et al. (1962).

The analytic fit of the differential ionization cross section of CO_2 due to proton impacts are taken from Rudd et al. (1983), including the production of 4 excited states ($X^2\Pi_g$, $A^2\Pi_u$, $B^2\Sigma_u^+$, and $C^2\Sigma_g^+$). The analytic fits of differential ionization cross sections of CO, N_2 and O_2 are also taken from Rudd et al. (1983). The total ionization cross section of O is taken from Basu et al. (1987) for above 2 keV and from Haider et al. (2002) for below 2 keV. The analytic fits of differential charge exchange cross sections of CO_2 above 10 keV are taken from Rudd et al. (1983), including the production of 4 excited states ($X^2\Pi_g$, $A^2\Pi_u$, $B^2\Sigma_u^+$, and $C^2\Sigma_g^+$). The total charge exchange cross section of CO_2 below 10 keV is taken from Haider et al. (2002), and the branching ratio is assumed to be the one for a 10 keV proton in Rudd et al. (1983). The analytic fits of differential charge exchange cross sections of CO, N_2 and O_2 are taken from Rudd et al. (1983). The total charge exchange cross section of O is taken from Basu et al. (1987) for above 1 keV and Haider et al. (2002) for below 1 keV.

Finally, we describe the elastic and inelastic cross sections due to hydrogen atom impacts. The total elastic cross sections are calculated by the formula of Noël and Prölss (1993), and the parameters for this formula are taken from Kallio and Barabash (2001). Since there is almost no information on the hydrogen atom-impact inelastic cross sections of

CO_2, we approximated these cross sections. The total ionization and electron stripping cross sections of CO_2 are assumed to be identical to the hydrogen atom impact total ionization and electron stripping cross section of O_2, as in many previous studies (e.g., Kallio and Barabash, 2001; Jolitz et al., 2017). The total ionization and electron stripping cross sections of O_2 are taken from Basu et al. (1987) for above 1 keV and from Haider et al. (2002) for below 1 keV. The branching ratio of CO_2^+ ($B^2\Sigma_u^+$) to total CO_2 ionization is assumed to be 0.1, which is identical to the branching ratio due to proton impacts (Rudd et al., 1983). The total ionization and electron stripping cross sections of CO are also assumed to be identical to those of O_2. The total ionization and electron stripping cross sections of N_2 are taken from Kozelov et al. (1992). The total ionization cross section of O is taken from Basu et al. (1987) for above 2 keV and Haider et al. (2002) for below 2 keV, and the electron stripping cross section of O is taken from Basu et al. (1987) for above 10 keV and from Haider et al. (2002) for below 10 keV. The cross section of CO_2 with hydrogen atoms leading to Lyman-α emission is taken from Haider et al. (2002).

2.3 Energy Loss, Scattering Angle, and Secondary Electron Energy

If a collision occurs, the energy loss, scattering angle and secondary electron energy are calculated for each type of collision. If a collision is elastic, the scattering angle and energy loss are calculated. The scattering angle distribution of electrons is taken from Porter et al. (1987) at low energy (CO_2: below 500 eV, CO: below 800 eV, O_2: below 500 eV, N_2: below 1 keV, and O: below 1 keV) and calculated by the formula of Yalcin et al. (2006) above these energies. The scattering angle of electrons is calculated randomly by using these scattering angle distributions (e.g., Solomon, 2001). The scattering angle of protons can be randomly calculated by using the differential elastic cross section in equation (2). The scattering angle distribution of hydrogen atoms is calculated by the formula of Noël and Prölss (1993), and the parameters for this formula are taken from Kallio and Barabash (2001). The scattering angle of hydrogen atoms is calculated randomly by using this scattering angle distribution (Noël and Prölss, 1993). Energy loss in elastic collision is calculated by solving equations of energy and momentum conservation in a binary collision.

If a collision is inelastic, incident particles lose a fixed amount of energy equal to the energy threshold for ionization, excitation, charge exchange, electron stripping and Lyman-α. Threshold energies are taken from the references of cross sections as already explained in the previous section. In all inelastic collisions, the scattering angle is assumed to be 0 with the assumption of strong forward-peaked scattering (Solomon,

2001). If a collision leads to ionization, the incident particle also loses the amount of energy associated with the produced secondary electron. Secondary electron energy due to an electron impact is randomly calculated by the formula of Green and Sawada (1972) and Jackman et al. (1977). The secondary electron energy due to a proton impact is randomly calculated by the formula of Solomon (2001). The secondary electron energy due to a hydrogen impact is also calculated by this method. If a collision leads to electron stripping from a hydrogen atom, the calculated secondary electron energy is in the rest frame of the hydrogen atom, which is then converted to the energy in the rest frame of the atmosphere. All the produced secondary electrons are added to the simulation. Electrons lose energy to thermal electrons via Coulomb collisions. The energy transfer rate from incident electrons to thermal electrons is calculated by the formula of Swartz et al. (1971).

2.4 Method for Converting Particle Trajectories into Flux

The collision rate as a function of altitude z for the jth collision type (e.g. ionization rate) of the sth atmospheric species in an SEP event, $P_s^j(z)$, can be calculated by integrating the collision rate of the incident flux of 1 cm^{-2} s^{-1} for incident energy E_0 as a function of altitude $p_s^j(z, E_0)$ weighted by the energy flux spectrum $f(E_0)$ cm^{-2} s^{-1} observed by MAVEN:

$$P_s^j(z) = \int f(E_0)\, p_s^j(z, E_0)\, dE_0 \qquad (5)$$

In the Monte Carlo model, the collision rate $p_s^j(z, E_0)$ can be calculated by counting the number of collisions leading to ionization with atmospheric particles in a given cell; however, this counting method is noisy at high altitudes where the collision frequency is small, and minor types of collisions that do not occur frequently. We convert the trajectories of all the particles into a flux and mean pitch angle of the incident particles as a function of altitude and energy. The ionization rate can then be calculated by using the flux, mean pitch angle, neutral density and collisional cross section. The flux and mean pitch angle are determined at each altitude z ($0 \le z \le 500$ km with 1 km resolution) and energy grid E ($15 \le E \le E_0$ eV, logarithmically spaced with 10 energy bins in one digit). The collision rate of the jth collision type of the sth atmospheric species within a cell of $[z, z+\Delta z]\times[E, E+\Delta E]$ of the incident energy E_0 with the incident flux at the top of the model of 1 cm^{-2} s^{-1}, $p_s^j(z, E_0)$ cm^{-3} s^{-1}, can be expressed by using the flux as:

$$p_s^j(z, E_0) = n_s(z) \int_0^{E_0} \sigma_s^j(E) \left[\frac{\phi^+(z, E, E_0)}{\bar{\mu}^+(z, E, E_0)} + \frac{\phi^-(z, E, E_0)}{\bar{\mu}^-(z, E, E_0)} \right] dE \qquad (6)$$

where $n_s(z)$ is the number density of the sth atmospheric species at the altitude grid of

z, $\sigma_s^j(E)$ is the cross section of the jth collision type of the sth atmospheric species at the energy grid of E, $\phi^+(z,E,E_0)$ and $\phi^-(z,E,E_0)$ are upward and downward fluxes with the incident flux of the incident energy E_0 at the top of the model of 1 cm^{-2} s^{-1} within a cell of $[z,z+\Delta z]\times[E,E+\Delta E]$, respectively, and $\bar{\mu}^+(z,E,E_0)$ and $\bar{\mu}^-(z,E,E_0)$ are the mean cosine pitch angles of upward and downward moving particles within a cell $[z,z+\Delta z]\times[E,E+\Delta E]$ for incident energy E_0, respectively.

We constructed a method of converting all particle trajectories into fluxes in the following flow: (1) converting the trajectory of a single particle into a flux and (2) taking the average of all the fluxes converted from each particle's trajectory. In Figure 2a, the red line illustrates the trajectory of a single particle in the altitude-energy frame. To convert the trajectory into a flux, one particle is injected (red dot in Figure 2a) per second, and all the particles follow the same trajectory. The flux is always 1 cm^{-2} s^{-1} at every point of the trajectory. In Figure 2b, the initial downward flux at the cell $[z,z+\Delta z]\times[E,E+\Delta E]$ is 1 cm^{-2} s^{-1} if a particle enters the cell $[z,z+\Delta z]\times[E,E+\Delta E]$ with negative vertical velocity, and vice versa. For better understanding, another example of a trajectory is shown in Figure 2c. The initial flux 1 cm^{-2} s^{-1} works well when a particle crosses the whole cell without being backscattered (an enlarged view of a cell in Figure 2g). The initial flux overestimates the flux if a particle does not cross the whole cell without being backscattered (e.g., a cell with a blue frame in Figure 2b and an enlarged view of a cell in Figure 2h), and underestimates the flux if it returns to the cell (e.g., a cell with a blue frame in Figure 2c and an enlarged view of a cell in Figure 2i) and if it is frequently backscattered within the cell (e.g., an enlarged view of a cell in Figure 2j), respectively. The overestimation and underestimation of the initial flux can be improved by multiplying the flux of 1 cm^{-2} s^{-1} by the ratio between the vertical length L traveled by the particle within the cell, and the vertical cell size Δz, $L/\Delta z$. The vertical length L within the cell can be calculated numerically by $L=\sum|v_{z_i}|\Delta t_i$ within the cell, where v_{z_i} is the vertical velocity of the ith particle and Δt_i is a time step size (Figure 2d). For example, for the downward flux, L is calculated numerically by summing $|v_{z_i}|\Delta t_i$ at each time step within the cell only if the particle moves downward ($v_{z_i}<0$). If a particle crosses the whole cell and is not backscattered into this cell, the flux is kept at 1 cm^{-2} s^{-1} (Figure 2g: L is the length of a vertical purple bar). If a particle does not cross the whole cell without being backscattered, the flux is then less than 1 (e.g., a cell with a blue frame in Figure 2e, and an enlarged view of a cell in Figure 2h: L is the length of a vertical purple bar). If a particle re-enters the cell or if it is frequently backscattered within the cell, the flux is then more than 1 cm^{-2} s^{-1} (e.g., a cell with a blue frame in Figure 2f, and

an enlarged view of a cell in Figure 2i and 2j: L is the sum of the length of vertical purple bars).

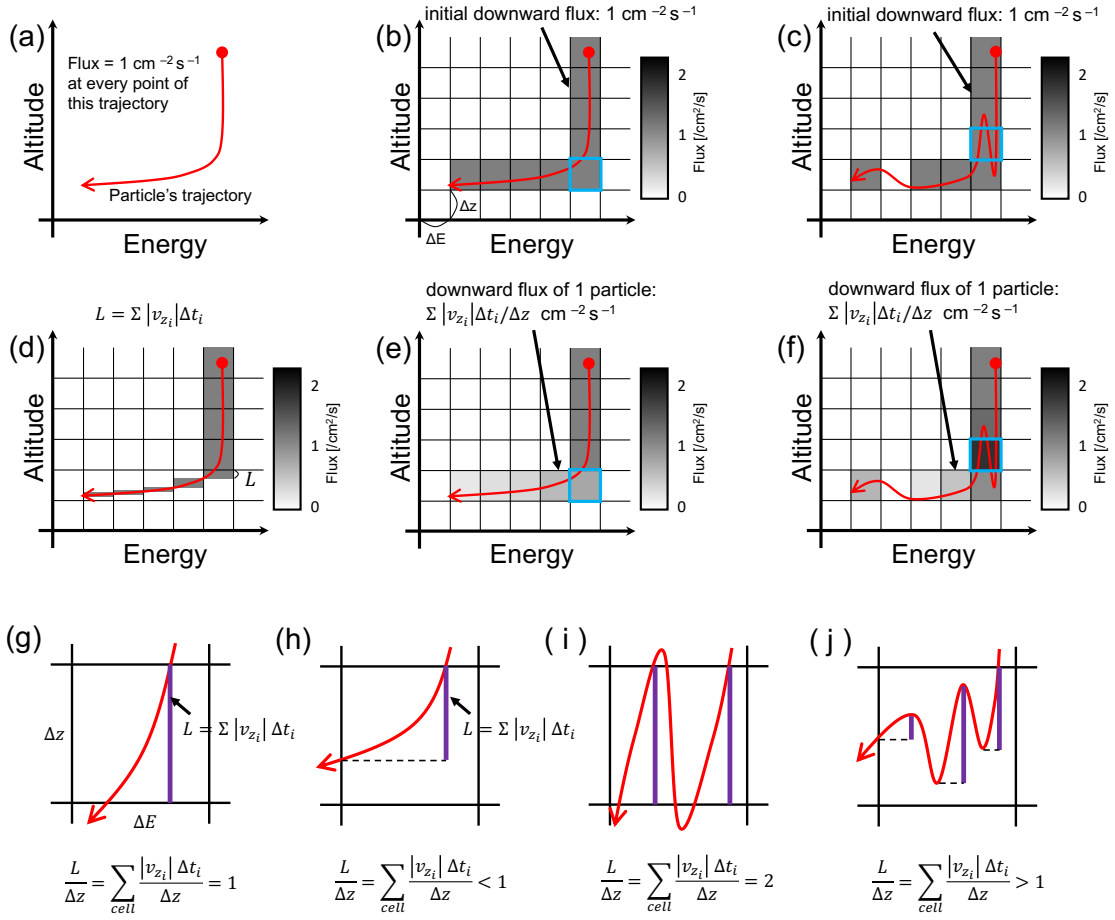


Figure 2 Schematic illustration of the method of converting the trajectory of a single particle (red lines) into a flux (see text for details). (g-j) The vertical purple bars represent the vertical length that traveled by a downward moving particle within the cell.

Finally, this flux of a single incident particle is calculated for each of the N incident particles, and taking average of all the converted fluxes yields the expressions of the upward and downward fluxes at each cell, corresponding to the flux of 1 cm^{-2} s^{-1} at the top of the atmosphere (Figure 2e and 2f). The upward and downward fluxes for an initial energy E_0 with the model topside incident flux of 1 cm^{-2} s^{-1} ($\phi^+(z, E, E_0)$ and $\phi^-(z, E, E_0)$, respectively) are expressed as:

$$\phi^{+}(z,E,E_0) = \frac{1}{N}\sum_{i=1}^{N} \sum_{\substack{z<z_i\le z+\Delta z \\ E<E_i\le E+\Delta E \\ v_{z_i}\ge 0}} \frac{|v_{z_i}|\Delta t_i}{\Delta z} \qquad (7)$$

$$\phi^{-}(z,E,E_0) = \frac{1}{N}\sum_{i=1}^{N} \sum_{\substack{z<z_i\le z+\Delta z \\ E<E_i\le E+\Delta E \\ v_{z_i}<0}} \frac{|v_{z_i}|\Delta t_i}{\Delta z} \qquad (8)$$

The upward and downward mean cosine pitch angles of the ith particle ($\bar{\mu}^{+}(z,E,E_0)$ and $\bar{\mu}^{-}(z,E,E_0)$) at the cell $[z,z+\Delta z]\times[E,E+\Delta E]$ are calculated by averaging the upward and downward cosine pitch angles, respectively. Averaging $\bar{\mu}^{+}(z,E,E_0)$ and $\bar{\mu}^{-}(z,E,E_0)$ for all particles that enter the cell $[z,z+\Delta z]\times[E,E+\Delta E]$ gives the mean cosine pitch angles of upward and downward particles $\bar{\mu}^{+}(z,E,E_0)$ and $\bar{\mu}^{-}(z,E,E_0)$, respectively. Examples of the calculated upward and downward fluxes, the mean cosine pitch angles, and a comparison of the two methods of deriving the ionization rate, counting the number of ionization collisions and using the converted fluxes, are shown in Figure S1-S5 in the supplementary materials. The ionization rate calculated by the method using the converted fluxes is in very good agreement with the counting method.

2.5 Limb Intensity of CO_2^+ UVD

The focus of this study is to derive the limb intensity profile of CO_2^+ UVD emissions. CO_2^+ UVD is emitted by the transition of CO_2^+ from the $B^2\Sigma_u^+$ state to the ground state $X^2\Pi_g$. The transition from CO_2^+ ($B^2\Sigma_u^+$) has another branch of transition to the $A^2\Pi_u$ state. We considered the branching ratio of the reaction leading to CO_2^+ UVD emission to be equal to 0.5 (Fox and Dalgano, 1979; Bhardwaj and Jain, 2013; Haider and Masoom, 2019). The CO_2^+ UVD volume emission rate is identical to the production rate of CO_2^+ ($B^2\Sigma_u^+$) multiplied by the branching ratio 0.5. The limb intensity profile of the CO_2^+ UVD volume emission rate, which can be directly compared to the observations by MAVEN/IUVS, is then calculated by integrating the CO_2^+ UVD volume emission rate along the line of sight in the limb geometry.

3. Instruments

The instruments used to constrain the electron and proton fluxes at the model topside are the Solar Energetic Particle (SEP) and Solar Wind Electron Analyzer (SWEA) onboard MAVEN.

The SEP instrument consists of two sensors: SEP1 and SEP2. Each sensor consists of a pair of double-ended solid-state telescopes to measure 20-1000 keV electrons and 20-6000 keV ions in four orthogonal directions with a field of view of 42° × 31° (Larson et al., 2015). The directions are labeled '1F', '1R', '2F' and '2R', where '1' and '2' denote the SEP instrument sensors (SEP1 and SEP2, respectively), and 'F' and 'R' denote the 'forward' FOV and 'reverse' FOV, respectively (Larson et al., 2015). The SEP instrument data used in this study correspond to Level 2 data provided by the Planetary Data System (PDS) (Larson et al., MAVEN SEP Calibrated Data Product Bundle, https://pds-ppi.igpp.ucla.edu/search/view/?f=yes&id=pds://PPI/maven.sep.calibrated/data/spec).

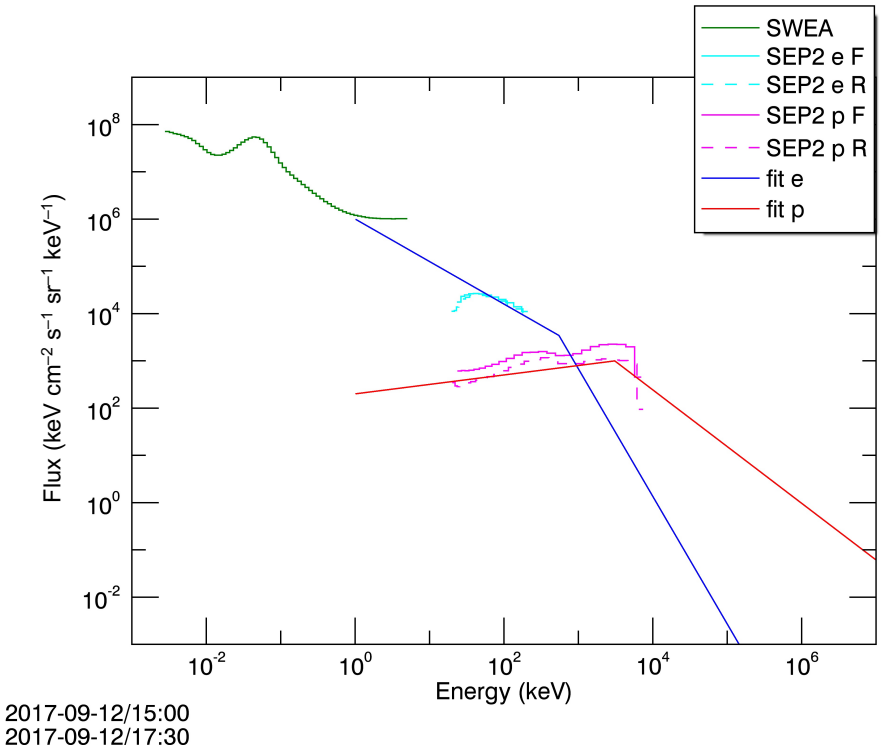
The SWEA instrument is a symmetric, hemispheric electrostatic analyzer designed to measure the energy and angular distributions of solar wind electrons and ionospheric photoelectrons in the Martian environment (Mitchell et al., 2016). The instruments measure electron fluxes in the energy range of 3 eV - 4.6 keV (Mitchell et al., 2016). The SWEA instrument data used in this study correspond to Level 2 data provided by the PDS (Mitchell et al., MAVEN SWEA Calibrated Data Bundle, https://pds-ppi.igpp.ucla.edu/search/view/?f=yes&id=pds://PPI/maven.swea.calibrated).

Note that we assume isotropic pitch angle distribution of electrons and protons obtained by SEP and SWEA. For electrons, we used SEP electrons > 30 keV and SWEA < 5 keV, with interpolation between those values. For protons, we used SEP ions > 50 keV because the sensitivity of the SEP ion is low below 50 keV.

We used the median value of the electron and proton fluxes obtained by SEP and SWEA instruments of the orbit 437 for the December 2014 SEP event. The orbit 437 was chosen because the observed auroral emission was the brightest (Schneider et al., 2015). The channel of the SEP instrument was selected as 1F; the electron and proton fluxes of the SEP instrument were used only when the SEP instrument attenuator was open. The electron and proton flux spectra for the December 2014 SEP event used in this study are shown in Figure 4 (a).

So far, the September 2017 SEP event has been the strongest solar energetic particle event detected by the SEP instrument at Mars. The high fluxes of energetic electrons and ions during this event caused the instrument mechanical attenuator to automatically close in order to reduce the detected flux of particles and prevent saturation of the instrument.

415 However, the flux of highest energy particles (above a few MeV) that can penetrate the
416 instrument housing (and the attenuator) was strong enough to contribute to a significant
417 portion of the differential energy flux measured by SEP at the range of energies that are
418 typically associated with particles that can be stopped by the attenuator. The level of
419 background is less severe for the time periods when the SEP attenuators were open so
420 that it was possible to apply fitting procedures in order to remove this background present
421 in the data. We fit a series of theoretical ion and electron spectra to the measurements in
422 all of the SEP energy channels, including coincidence events that are mainly caused by
423 penetrating particles. In our fitting, we use a realistic model of the instrument geometric
424 factor and find the ion and electron spectra that produce the best match with the
425 measurements. The results are shown in Figure 3. The electron and proton flux spectra
426 for the September 2017 SEP event used in this study are shown in Figure 4 (b). Note that
427 since the electron and proton fluxes used for the September 2017 SEP event was taken
428 from the timing just before the flux peak and auroral emission peak, the resulting modeled
429 auroral emission intensity should be small compared with the IUVS observation reported
430 by Schneider et al. (2018). For this event, we do not focus on the absolute auroral
431 emission intensity but on the relative intensity of electron- and proton- induced emissions
432 and on the shapes of the auroral emission profiles.
433



434
435 Figure 3 Electron and proton fluxes measured by SEP and SWEA

/MAVEN from 15:00UT to 17:30UT on 12 September 2017. Green line shows the electron flux observed by SWEA. The cyan solid and dashed lines show the electron fluxes observed by the SEP2 sensor in the forward and in the reverse directions, respectively. The violet solid and dashed lines show the proton fluxes observed by the SEP2 sensor in the forward and in the reversed directions, respectively. The blue solid line is the fit used in this paper for the electron fluxes and the red solid line is that for the proton fluxes.

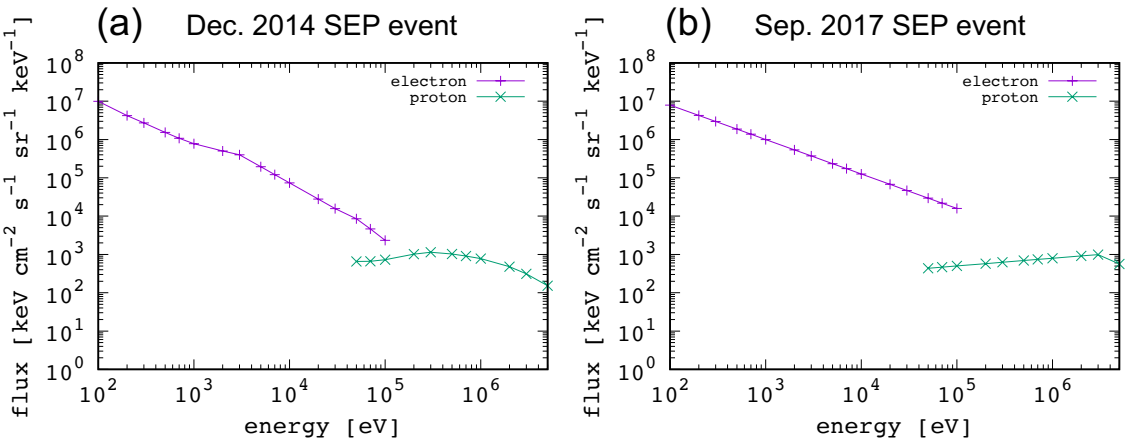


Figure 4 (a, b) Electron and proton fluxes for the December 2014 SEP event and the September 2017 SEP event that were used in this study, respectively.

4. Results

4.1 Validation

Since the numerical codes of PTRIP were newly developed, we first compare our model of electron transport with Gérard et al. (2017). The altitude profile of CO_2 is taken from Gérard et al. (2017). For simplicity, we ignore other species of the atmosphere in this test calculation. Our model uses the scattering angle distributions for elastic scattering with the CO_2 of Porter et al. (1987) for below 500 eV and that of Yalcin et al. (2006) for above 500 eV. Since Gérard et al. (2017) used the value of Porter et al. (1987) even at high energies, we performed validation calculations for two cases: (1) case 1 used the Porter et al. (1987) scattering angle distribution at all energies, and (2) case 2 used the Porter et al. (1987) value for below 500 eV and the Yalcin et al. (2006) value for above 500 eV.

The electron flux at the top of the model is 1 mW m^{-2} for all incident energies, which is set to be the same as Gérard et al. (2017). The incident angle is isotropically distributed.

Figure 5 (a, b) shows the calculated CO_2^+ ($B^2\Sigma_u^+$) production rate for the two cases, and (c, d) shows the calculated limb intensity of CO_2^+ UVD for the two cases. In case 1, the production rate of CO_2^+ ($B^2\Sigma_u^+$) and the limb intensity of CO_2^+ UVD are the largest at 2 keV and decrease with incident energy above 2 keV. This trend is also visible with the Gérard et al. (2017) value. The peak limb intensity of CO_2^+ UVD in case 1 is 30 kR at 2 keV and 10 kR at 100 keV, which is in good agreement with Gérard et al. (2017). In case 2, the production rate of CO_2^+ ($B^2\Sigma_u^+$) and limb intensity of CO_2^+ UVD are almost constant above 500 eV. The production rate of CO_2^+ ($B^2\Sigma_u^+$) at 100 keV in case 1 is 4 times smaller than that in case 2. The penetration altitude of electrons in case 1 is higher than that in case 2. The difference between the two cases comes from the different scattering angle distributions. Figure 6 shows the backscatter probability of electrons at each incident energy for the two cases. In case 1, the backscatter probability increases with incident energy above 500 eV and reaches ~80% at 100 keV. In case 2, the backscatter probability is almost constant at ~ 30% above 2 keV. In case 1, since the same scattering angle distribution is used above 500 eV, electrons with higher energy have more chances to change of direction because they experience more elastic collisions. In case 2, since scattering becomes more forward-peaked at high energy, the backscatter probability does not increase at high energy. The production rate of CO_2^+ ($B^2\Sigma_u^+$) and limb intensity of CO_2^+ UVD in case 1 at high energy are smaller than those in case 2 because electrons are more likely to be backscattered before they lose energy via ionization. There remains discrepancy in the penetration altitude of electrons between case 1 and Gérard et al. (2017); the possible reasons are the different total elastic cross section and ionization cross section used in the two models. However, the penetration altitude of electrons during the December 2014 SEP event in our calculation (in case 2) is consistent with Haider and Masoom (2019), as explained in Section 4.2.

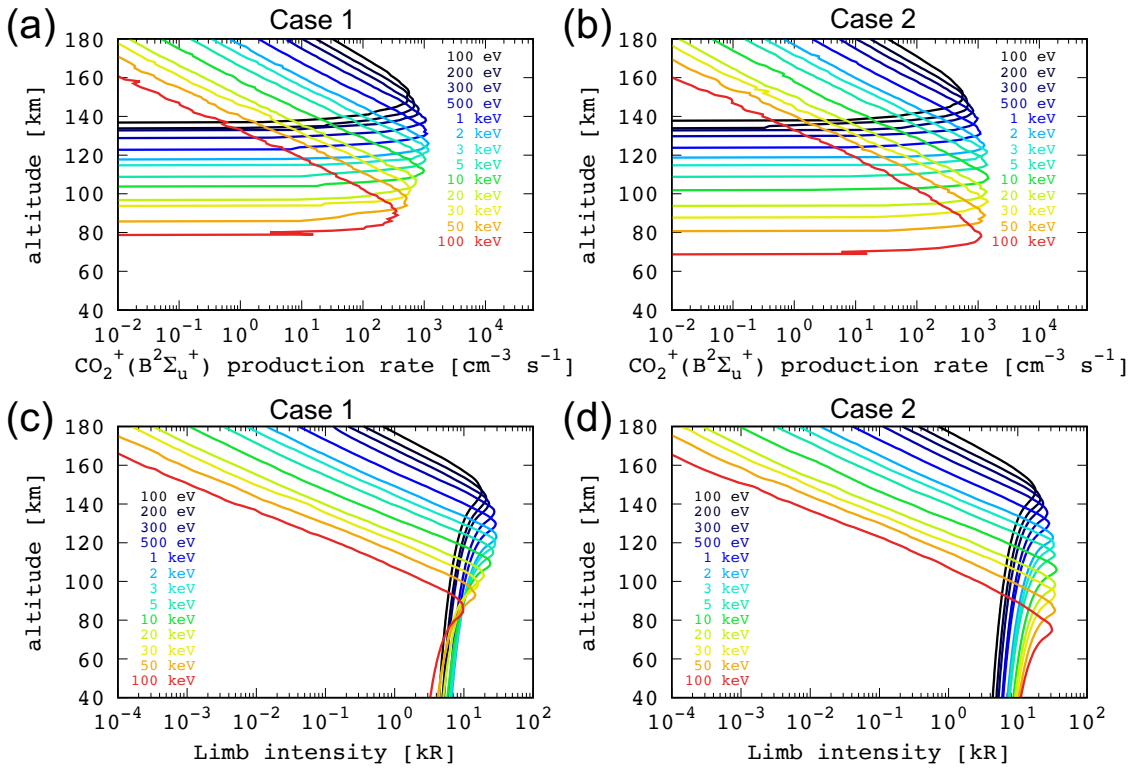


Figure 5 (a, b) Production rate of CO_2^+ ($B^2\Sigma_u^+$) due to electron impacts for each incident electron energy in case 1 and case 2. Case 1 uses the elastic scattering angle distribution of Porter et al. (1987) for all energies, and case 2 uses Porter et al. (1987) below 500 eV and Yalcin et al. (2006) above 500 eV. (c, d) Limb intensity profile of CO_2^+ UVD in case 1 and case 2, respectively. The model topside incident electron flux is 1 mW m^{-2} at each incident energy for the two cases.

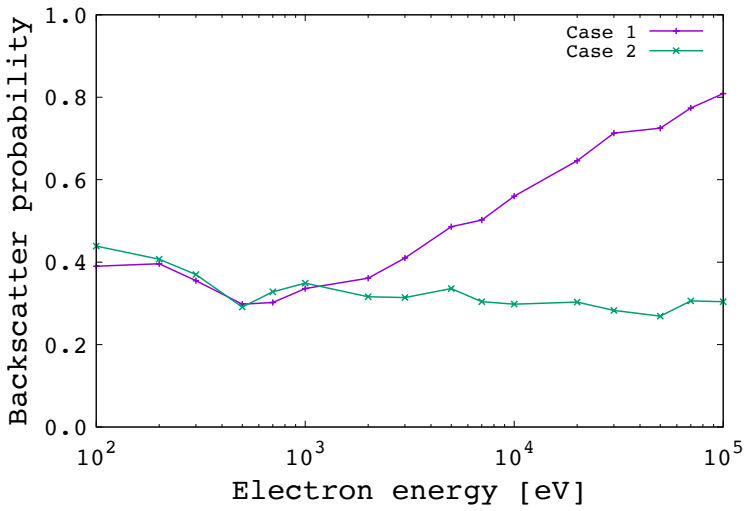


Figure 6 Backscatter probability of different incident electron energies in case 1 and case 2.

Our model of proton and hydrogen atom transport is also compared with previous models. Several models have been proposed for proton and hydrogen atom transport in the Martian atmosphere: a model of fast neutral hydrogen atoms (hereafter called KB01) (Kallio and Barabash, 2001), the Stopping and Range of Ions in Matter model (hereafter called SRIM) (Leblanc et al., 2002), and the Atmospheric Scattering of Protons and Energetic Neutrals (hereafter called ASPEN) (Jolitz et al., 2017). KB01, SRIM and ASPEN were previously compared in Leblanc et al. (2002) and Jolitz et al. (2017) using the test calculation of incident 800 eV neutral hydrogen atoms. One thousand hydrogen atoms of 800 eV were isotropically injected into the Martian atmosphere. Our model predicts that 27% of the energy is deposited into ionization, which agrees with KB01 (27%) and ASPEN (26%). We found that 26% and 24% of energy is deposited into electron stripping and Lyman-α emission, respectively, which agree with KB01 (26% and 30%, respectively). We found that 19% of the energy was deposited into direct neutral heating via elastic collision, which is in close agreement with KB01 (14%), SRIM (16%) and ASPEN (13%). Our model found that 57% of hydrogen atoms were backscattered, which agrees with KB01 (58%) and is larger than ASPEN (32%) and SRIM (10%).

For proton transport, our model uses the differential and the total elastic cross sections

described in equations (2) and (4), while ASPEN used the differential and the total elastic cross sections from KB01, and it predicted that the backscatter probability of protons increases with incident energy above 100 keV, reaching more than 60% at 5 MeV. Since they used the scattering angle distribution from KB01 that does not depend on the proton energy, higher energy protons experience so many elastic collisions that they are more likely to change of direction. We tested the proton backscatter probability for two cases: case A used the same differential and total elastic cross section of protons and hydrogen atoms as KB01, and case B used the differential and total elastic cross section of protons described in equations (2) and (4) and those of hydrogen atoms from KB01. The backscatter probabilities of different incident proton energies in the two cases are shown in Figure 7. In case A, the backscatter probability of protons increases with incident proton energy above 200 keV and reaches more than 60% at 5 MeV, which is in close agreement with ASPEN. In case B, the backscatter probability is close to that in case A below 100 keV, but it decreases with incident proton energy and reaches nearly 0% at 5 MeV because the scattering becomes more likely to be forward-peaked at higher energy. As described in Section 2.2, since KB01 overestimated the differential elastic cross section of MeV protons by a few orders of magnitude at large scattering angles, case A significantly overestimated the backscatter probability, which leads to the underestimation of the ionization rate at low altitudes where MeV protons deposit energy into the atmosphere.

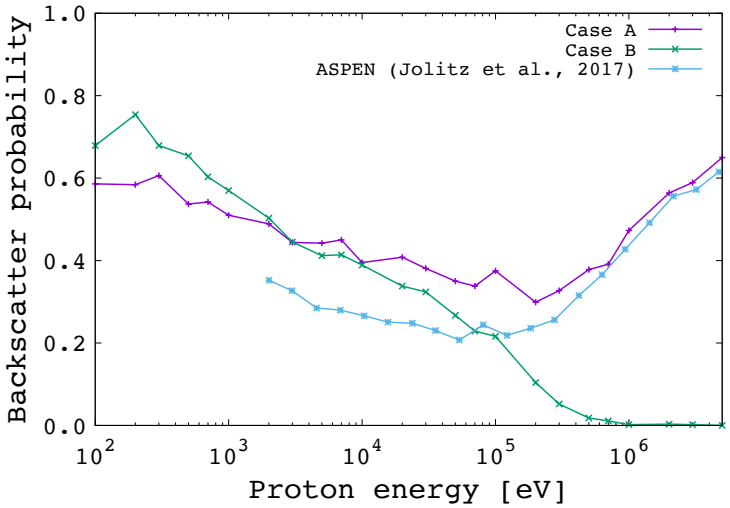


Figure 7 Backscatter probability of different incident proton energies in case A and case B. Case A uses the differential cross section, and the total elastic cross section from KB01 and case B uses the screened Rutherford

elastic cross section.

4.2 Production Rate of CO_2^+ ($B^2\Sigma_u^+$) During SEP Events

Figure 8 represents the calculated production rate of CO_2^+ ($B^2\Sigma_u^+$) with an incident flux of 1 cm^{-2} s^{-1} at each incident energy of electrons and protons at the top of the model on 20 December 2014 and on 13 September 2017. The penetration altitude of electrons in our calculation was compared with Haider and Masoom (2019). They calculated the ionization rate during the December 2014 SEP event and found that the ionization rate by 100 keV electrons peaks at an altitude of 75 km. The peak altitude of the ionization rate by 100 keV electrons is 75 km in our model, which is precisely consistent with Haider and Masoom (2019). For protons, the penetration altitude of 5 MeV protons is approximately 55-65 km, which is approximately 10-20 km higher than Jolitz et al. (2017). The possible reasons for the discrepancy between our model and Jolitz et al. (2017) are the different atmospheric density profiles, which are not described in Jolitz et al. (2017). Different scattering angle distributions in the elastic collision can also explain this discrepancy with Jolitz et al. (2017) because the smaller differential elastic cross section at a large scattering angle used in PTRIP implies a smaller deviation of the protons when traveling radially and therefore a deeper penetration.

The penetration altitude at each incident energy is approximately 10 km lower for the September 2017 SEP event than for the December 2014 SEP event. The Ls was 255° (near perihelion) on 20 December 2014 and 60° (near aphelion) on 13 September 2017, corresponding to the season of atmospheric inflation and contraction on Mars, respectively (e.g., Forget et al., 2009).

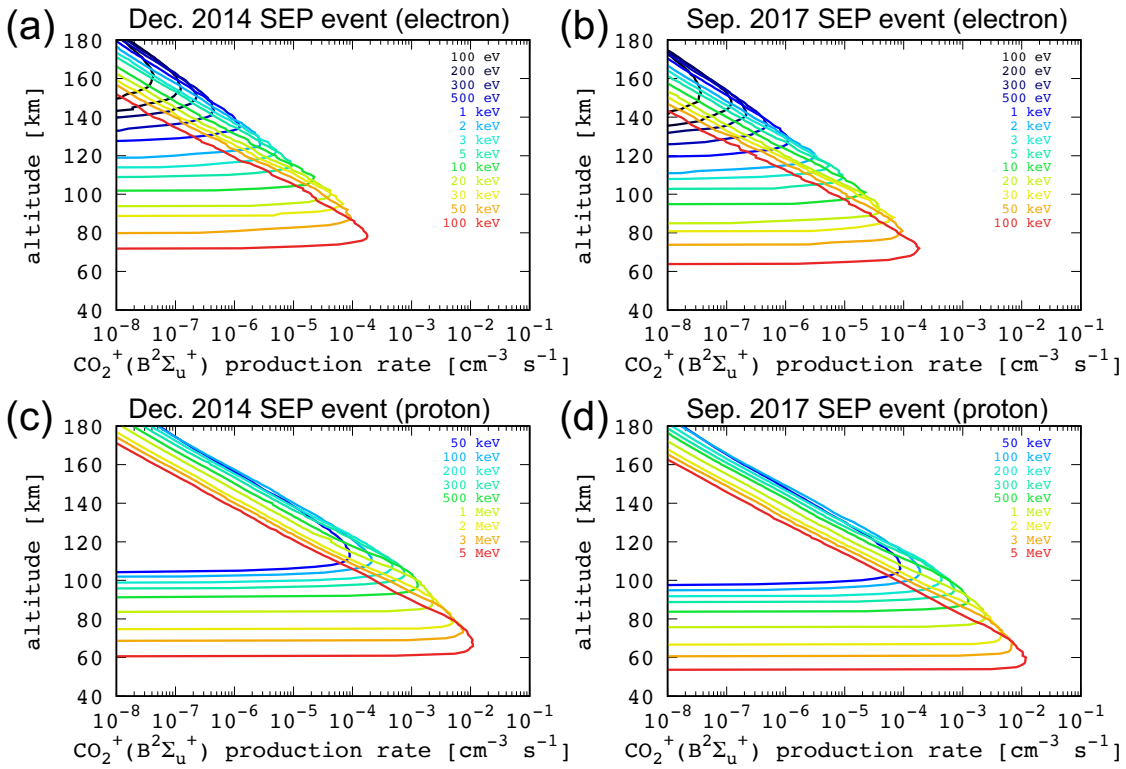


Figure 8 (a, b) Production rate of CO_2^+ ($B^2\Sigma_u^+$) with an incident flux of 1 cm^{-2} s^{-1} for each incident energy of electrons at the top of the model during the December 2014 SEP event and September 2017 event, respectively, and (c, d) those of protons during the December 2014 SEP event and September 2017 SEP event, respectively. Note that not all incident energies in the model are shown here to make the figure easier to read.

Figure 9 shows the calculated production rate of CO_2^+ ($B^2\Sigma_u^+$) for each incident energy of electrons and protons during the December 2014 SEP event and September 2017 SEP event according to equation (5) by using the production rate with an incident flux of 1 cm^{-2} s^{-1} at each incident energy (Figure 8) and electron and proton fluxes observed by MAVEN (Figure 4). A comparison of the total production rate of CO_2^+ ($B^2\Sigma_u^+$) between incident electrons and protons during these two SEP events is shown in Figure 10. During the SEP event in December 2014, the largest contribution to the production rate of CO_2^+ ($B^2\Sigma_u^+$) due to electron impact occurs at an altitude of approximately 110 km, corresponding to the incident 3-10 keV electrons (Figure 9a). The largest contribution to the production rate of CO_2^+ ($B^2\Sigma_u^+$) due to proton and hydrogen atom impacts occurs at

80 km altitude by incident 2 MeV protons (Figure 9c). The production rates of CO_2^+ ($B^2\Sigma_u^+$) by electrons and protons both have a peak value of 10 cm^{-3} s^{-1} during this SEP event. During the SEP event in September 2017, the largest contribution to the production rate of CO_2^+ ($B^2\Sigma_u^+$) due to electron impact occurs at 70 km altitude by incident 100 keV electrons. The largest contribution to the production rate of CO_2^+ ($B^2\Sigma_u^+$) due to proton and hydrogen atom impacts occurs at 70 km altitude by incident 3 MeV protons. The production rate of CO_2^+ ($B^2\Sigma_u^+$) by electrons and protons has peak values of 20 cm^{-3} s^{-1} and 40 cm^{-3} s^{-1}, respectively. For both SEP events, the production rate of CO_2^+ ($B^2\Sigma_u^+$) is dominated by proton impacts below 100 km altitude and by electron impacts above 100 km. It is noted that the limitation of the energy range of PTRIP could affect our simulation of the September 2017 SEP event. The production rate of CO_2^+ ($B^2\Sigma_u^+$) due to precipitation of both electrons and protons increases with an incident energy up to near the upper limit of the energy range of the calculation. A higher energy than considered in our model would increase the CO_2^+ ($B^2\Sigma_u^+$) production rate at lower altitudes, which could result in a lower peak altitude and a larger peak production rate than that shown in Figure 10. Incident energy of protons are limited above 50 keV due to the observational limitation of the SEP instrument. Protons below 50 keV could contribute to the production of CO_2^+ ($B^2\Sigma_u^+$) at altitudes above ~110 km, but their contribution can simply be speculated to be less than 1/100 of the peak value due to MeV protons according to Figure 9.

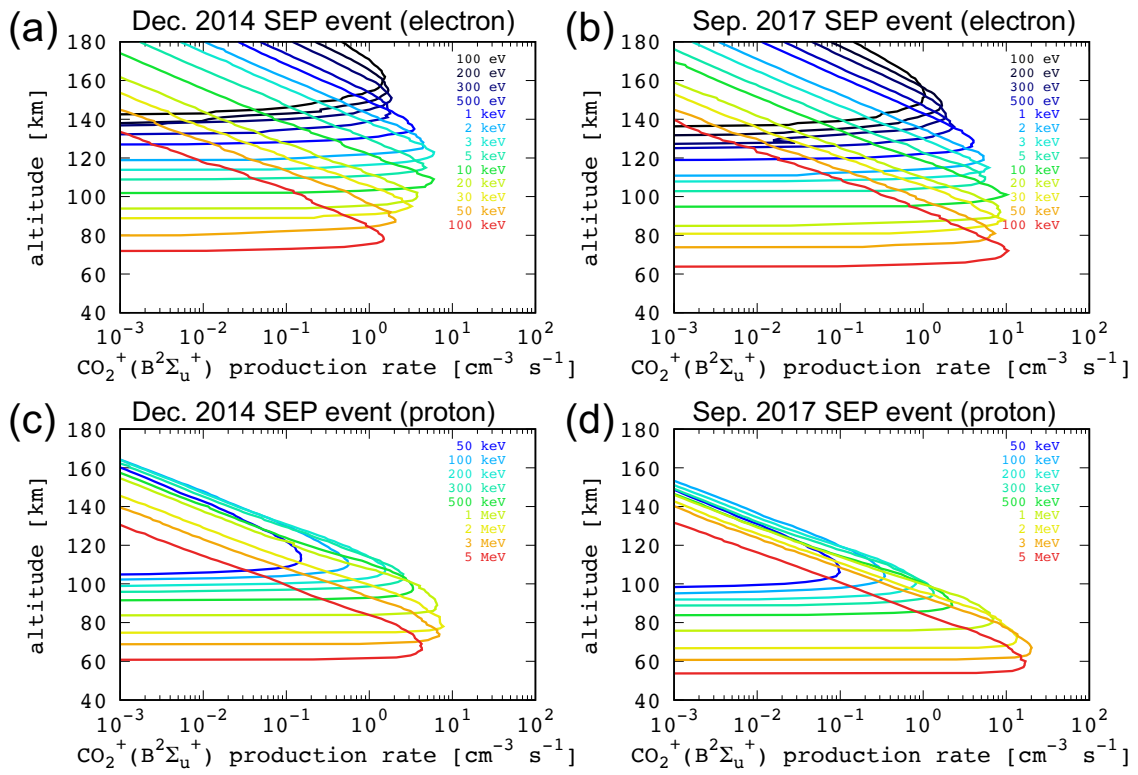


Figure 9 (a, b) Production rate of CO_2^+ ($B^2\Sigma_u^+$) due to precipitation of electrons during the December 2014 SEP event and September 2017 event, respectively, and (c, d) those of protons during the December 2014 SEP event and September 2017 SEP event, respectively. These production rates are calculated by using the energy flux observed by MAVEN/SEP and SWEA. Note that not all incident energies in the model are shown here to make the figure easier to read.

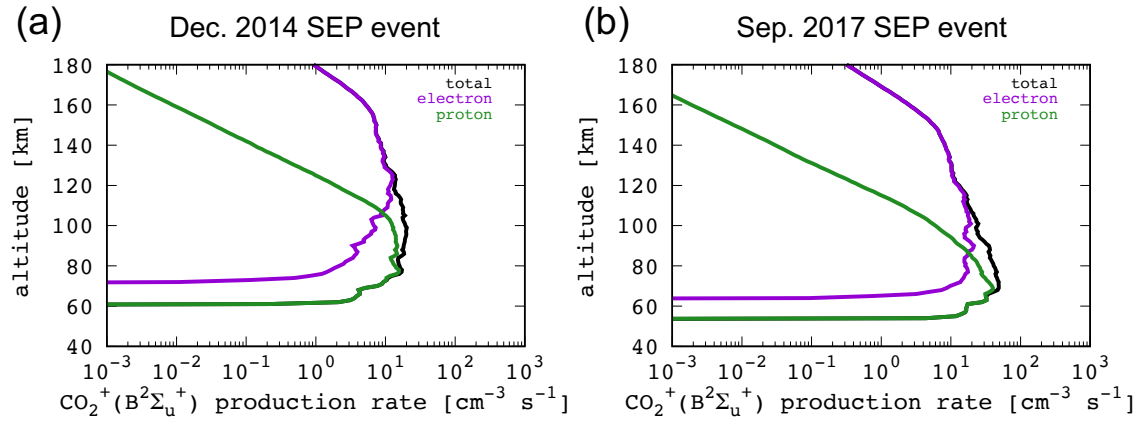


Figure 10 (a, b) Total production rate of CO_2^+ ($B^2\Sigma_u^+$) (black) and the

contribution of impacting electrons (purple) and protons (green) during the December 2014 SEP event and September 2017 SEP event, respectively.

4.3 CO_2^+ UVD Limb Intensity Profiles During SEP Events

The limb intensity profile of CO_2^+ UVD emissions is calculated by integrating the volume emission rate of CO_2^+ UVD along the line of sight in the limb geometry. As mentioned in Section 2.5, the volume emission rate of CO_2^+ UVD is estimated by multiplying the production rate of CO_2^+ ($B^2\Sigma_u^+$) by 0.5. Figure 11 shows the limb intensity profile of CO_2^+ UVD for each incident energy of electrons and protons during the December 2014 SEP event and September 2017 SEP event.

During the SEP event in December 2014, electron-induced CO_2^+ UVD emissions are largest at approximately 110 km with an intensity of 1 kR, produced essentially by 3-10 keV electrons. As suggested by previous models of diffuse aurora during the December 2014 SEP event (Schneider et al., 2015; Gérard et al., 2017; Haider and Masoom, 2019), 100 keV electrons reasonably produce CO_2^+ UVD emissions at low altitudes (70-80 km), as observed by MAVEN; however, the total electron-induced emissions do not peak at low altitudes because low-energy electrons produce brighter emissions at higher altitudes. While electron-induced CO_2^+ UVD emission peaks at a high altitude of ~110 km, proton-induced CO_2^+ UVD emission peaks at a low altitude of ~80 km with an intensity of 1 kR due to 1 MeV protons.

During the September 2017 SEP event, electron-induced CO_2^+ UVD emissions are largest at approximately 70 km with an intensity of 1 kR due to 100 keV electrons. Proton-induced CO_2^+ UVD emission peaks at low altitudes of ~65 km with an intensity of 2 kR due to 3 MeV protons. For both SEP events, the electron-induced CO_2^+ UVD emission profile covers an altitude range between 60 and 140 km, while the proton-induced CO_2^+ UVD emission profile has a narrower altitude range (between 60 and 100 km) owing to the difference in the electron and proton spectral shape as shown in Figure 4.

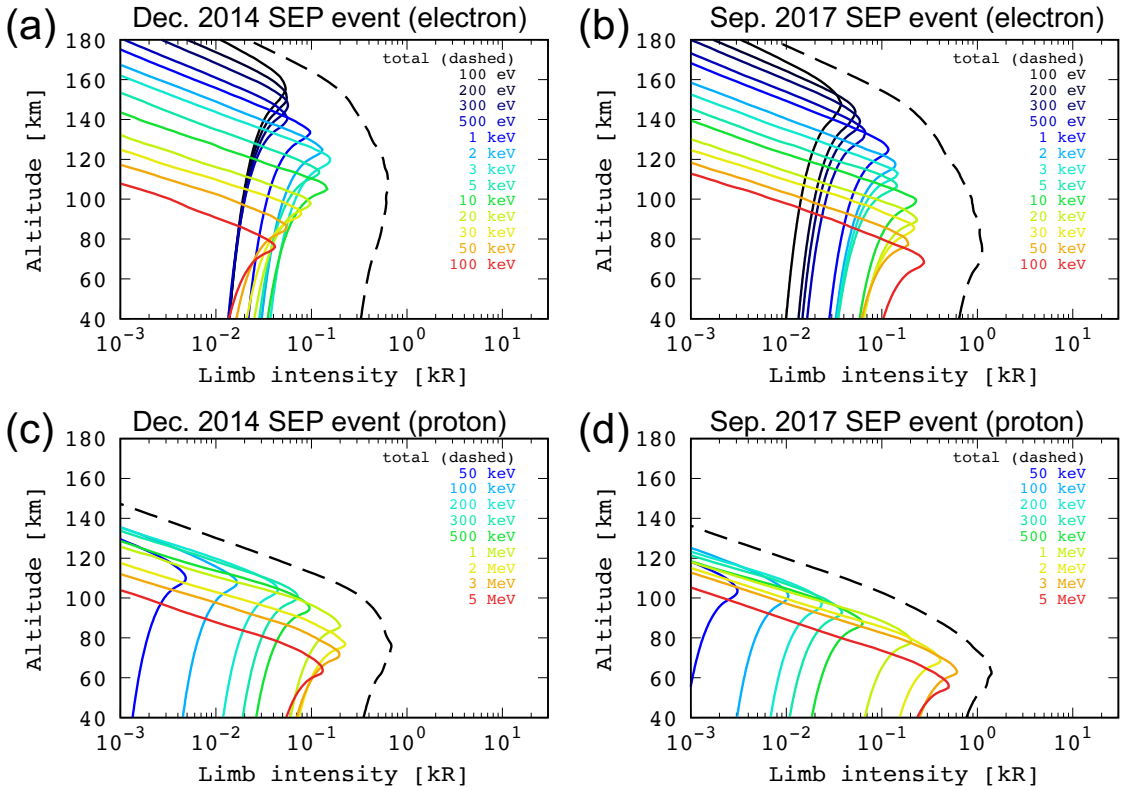


Figure 11 (a, b) Limb intensity of CO_2^+ UVD due to precipitation of electrons for differential incident energies during the December 2014 SEP event and September 2017 SEP event, respectively, and (c, d) those of protons during the December 2014 SEP event and September 2017 SEP event, respectively. Note that not all incident energies in the model are shown here to make the figure easier to read.

We compared our model results with the observations of CO_2^+ UVD limb intensity obtained by Schneider et al. (2015) and Schneider et al. (2018) for the December 2014 SEP event and September 2017 SEP event, respectively. Figure 12 (a) shows the calculated limb intensity profile of CO_2^+ UVD emissions and the observed profiles during the SEP event in December 2014. The calculated total CO_2^+ UVD limb intensity is 2 times larger than the observation. Our calculated altitude profile peaks at 76 km, which is very close to the observed peak at ~70 km. Figure 12 (b) shows the calculated limb intensity profile of CO_2^+ UVD emissions and the observed profiles during the SEP event in September 2017. Since we used the electron and proton flux at the time before the flux peak and auroral emission peak, the calculated limb profiles were multiplied by a factor

of 8 to match the observed emission intensity. Our calculated altitude profile peaks at 68 km, which is 10 km higher than the observation.

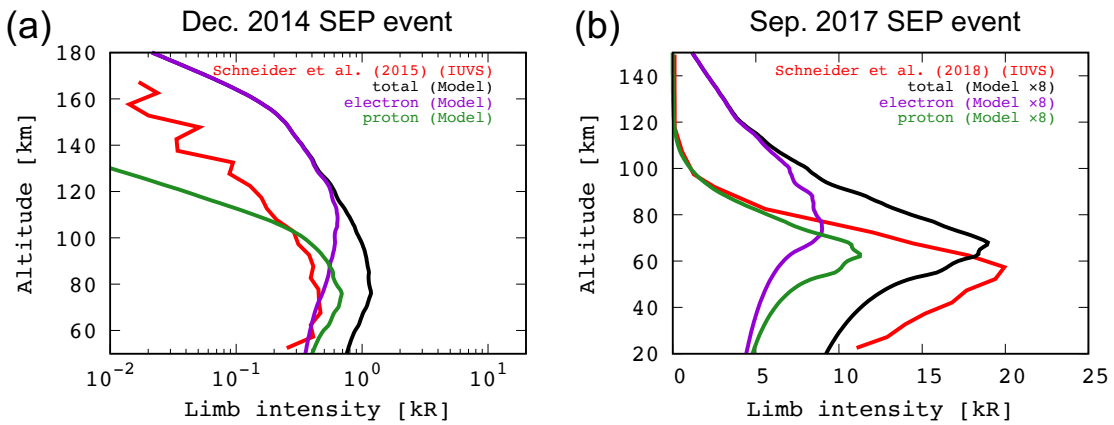


Figure 12 (a, b) Total limb intensity of CO_2^+ UVD (black) and contribution of impacting electrons (purple) and protons (green) during the December 2014 SEP event and September 2017 SEP event, respectively. Observed profiles are taken from Schneider et al. (2015) and Schneider et al. (2018) in the December 2014 SEP event and September 2017 SEP event, respectively. Note that the calculated limb profiles for the September 2017 SEP event were multiplied by a factor of 8 to match the observed emission intensity.

5. Discussion

Even if we found a good agreement between observations and simulations (Figure 12), there are several limits when comparing modeled with observed profiles. The results displayed in Figure 12 depend first on the cross sections and ionizing branching ratio of the H-CO_2 collision. Since we assumed that most of the cross sections for H-CO_2 used are identical to the cross sections for H-O_2 collisions, our calculations might be impacted by this assumption. Another aspect that may have affected our calculations is that we assumed the branching ratio of CO_2^+ ($B^2\Sigma_u^+$) to the total CO_2 ionization due to hydrogen atom impacts to be 0.1.

As already mentioned in Section 4.2, the upper limit of the energy range considered in PTRIP could limit our capability to compare the results of our simulation to the IUVS observations. Extrapolating the cross sections (see Text S1 in the supplementary materials) and the electron and proton flux considered in this paper allow us to provide a

first estimate of the potential contributions to the emission due to electrons above 100 keV and protons above 5 MeV. For the December 2014 SEP event, since the electron and proton fluxes observed by MAVEN/SEP is limited below 200 keV and 6 MeV, respectively, we simply extrapolated the electron flux above 200 keV and proton flux above 6 MeV logarithmically to estimate the contribution of energetic electrons up to 500 keV and energetic protons up to 20 MeV. For the September 2017 SEP event, fitting results of the electron and proton fluxes shown in Figure 3 was used to estimate the contribution of energetic electrons up to 500 keV and energetic protons up to 20 MeV. Figure 13 shows the limb intensity profile of CO_2^+ UVD for each incident energy of electrons up to 500 keV and protons up to 20 MeV during the December 2014 SEP event and September 2017 SEP event. During the December 2014 SEP event, contribution of electrons above 100 keV is comparatively small, while the contribution of protons above 5 MeV is comparable to the peak value. During the September 2017 SEP event, contribution of both electrons above 500 keV and protons above 5 MeV are comparable to the peak value. A comparison between our model results with energy extension and the IUVS observations is shown in Figure 14. Note that the calculated limb profiles for the September 2017 SEP event were multiplied by a factor of 6 to match the observed emission intensity. During the December 2014 SEP event, the shapes, the peak altitude and the intensity of CO_2^+ UVD limb profiles does not largely change even if we take into account the contribution of more energetic electrons and protons. During the September 2017 SEP event, the calculated limb intensity profile changed below 70 km altitude and it peaks at 55 km, which is in good agreement with the IUVS observation.

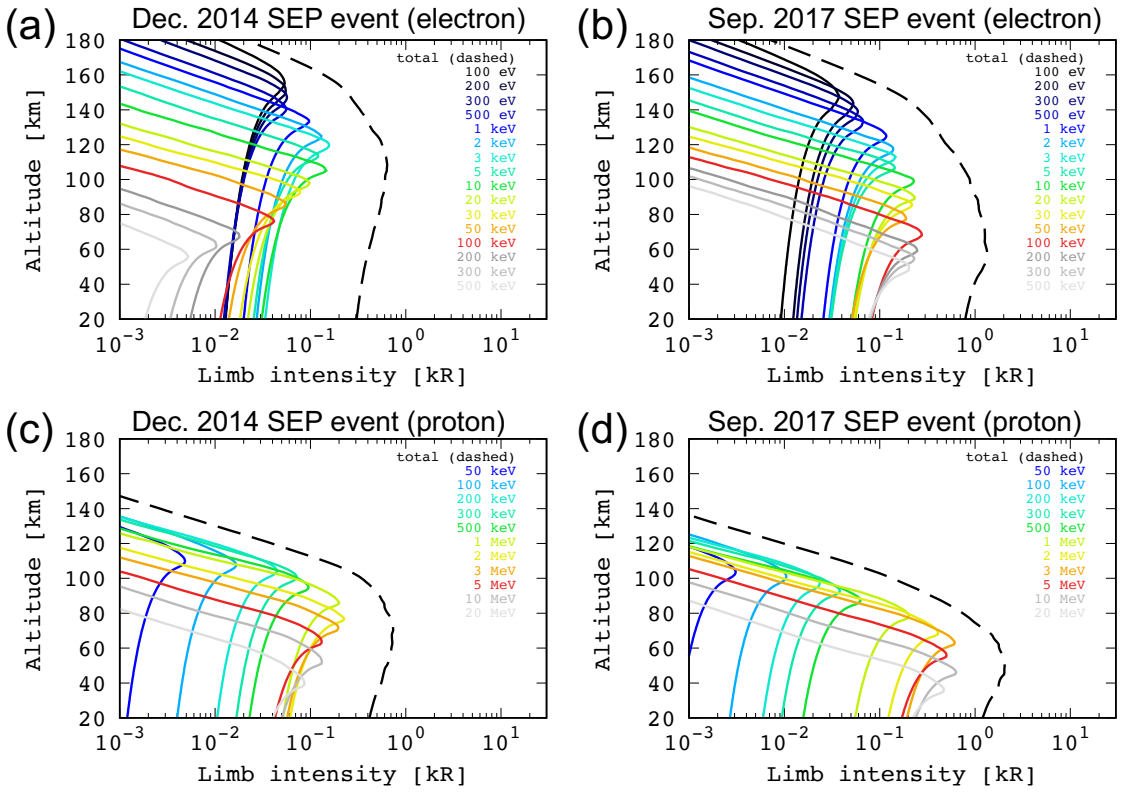


Figure 13 (a, b) Limb intensity of CO_2^+ UVD due to precipitation of electrons for differential incident energies during the December 2014 SEP event and September 2017 SEP event, respectively, and (c, d) those of protons during the December 2014 SEP event and September 2017 SEP event, respectively. Electron and proton energy ranges are extended to 500 keV and 20 MeV, respectively. Note that not all incident energies in the model are shown here to make the figure easier to read.

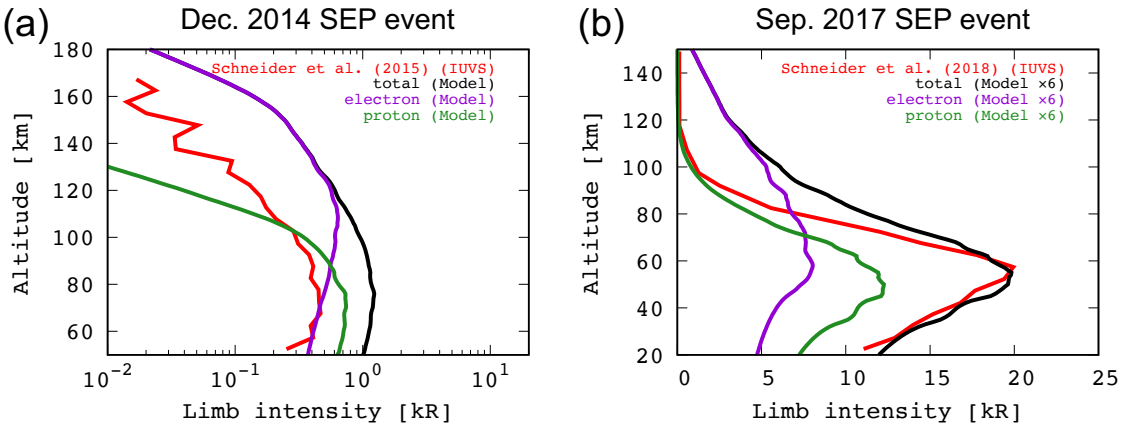


Figure 14 (a, b) The contribution of impacting electrons up to 500 keV (purple) and protons up to 20 MeV (green) to the CO_2^+ UVD limb intensity, and the total limb intensity of CO_2^+ UVD (black) during the December 2014 SEP event and September 2017 SEP event, respectively. Observed profiles are taken from Schneider et al. (2015) and Schneider et al. (2018) in the December 2014 SEP event and September 2017 SEP event, respectively. Note that the calculated limb profiles for the September 2017 SEP event were multiplied by a factor of 6 to match the observed emission intensity.

The penetration altitude of incident particles strongly depends on the neutral atmospheric temperature. The Martian atmosphere is known to exhibit large variability with respect to season, latitude and local time (e.g., Forget et al., 2009). A different atmospheric temperature would impact, as a first order, the altitude profile of the emission brightness. Since we obtained rather good agreement between the simulated altitude profile of the emission brightness and the observed profile for the two SEP events, our choice of atmospheric density profiles for both events were close to the real atmospheric conditions at that time.

We did not take into account the effects of the magnetic field. Electrons are expected to be guided to the regions of open magnetic field lines, and they are unlikely to penetrate into close field line regions (Lillis et al., 2011; Jolitz et al., 2021). Proton penetration to low altitudes is also expected to be depleted in regions of strong crustal fields (Leblanc et al., 2002). Due to the different gyro radii of electrons and protons, different sensitivities to the magnetic field strength and configuration are expected (Bisikalo et al., 2017).

We provide possible explanations for the overestimation of the modeled CO_2^+ UVD limb intensity compared to the IUVS observations. Since the SEP-induced CO_2^+ UVD emission peaks at low altitudes, CO_2^+ UVD could have been absorbed by the Martian atmosphere if there is an absorber of CO_2^+ UVD. Ozone has a strong absorption line around the wavelength of CO_2^+ UVD ~289 nm. The absorption cross section of ozone at 289 nm is about 10^{-22} m^2 (Gröller et al., 2018) and the maximum density of ozone is 10^{15} m^{-3} above an altitude of 50 km (Lebonnois et al., 2006). Integrating the optical depth along the line of sight over a distance of 1000 km using the above cross section and density of ozone yields an upper limit of the optical depth of 0.1 at 289 nm, which is

insufficient to absorb CO_2^+ UVD emission by the Martian atmosphere above an altitude of 50 km.

SEP shadowing by Mars could reduce the SEP ion flux on the nightside of Mars. The Martian Radiation Environment Experiment (MARIE) measurements onboard Mars Odyssey found that the count rate of SEP ions (20-200 MeV) near Mars showed modulation during solar events in October 2002 (Luhmann et al., 2007). They showed that the modulation of the SEP ion flux near Mars resulted from the shadowing of the SEP ion flux and the orientation of the interplanetary magnetic field (IMF). Lillis et al. (2016) reported the anisotropy of SEP ions near Mars, which was suggested to be caused by shadowing by Mars and the configuration of the magnetic field. Since the location and the timing of the observation of electron and proton fluxes made by MAVEN/SEP and SWEA were not precisely the same as the observations of the auroral emission made by MAVEN/IUVS, SEP shadowing might have reduced fluxes at the origin of IUVS observations. Shadowing of the SEP event by Mars might largely explain the factor of 2 of the difference between the observed emission brightness and the simulated brightness at the SEP event on 20 December 2014. Another aspect that might reduce the model emission rate is the calculation geometry. Our calculation used the plane-parallel atmosphere, but if we apply a spherical atmosphere, MeV protons with pitch angles larger than 60 degrees at an altitude of 500 km do not penetrate deep into the atmosphere but go through the upper atmosphere and exit the atmosphere because of their gyro radii, which are on the order of the planetary radius. The geometric effect is effective for only protons with energies larger than MeV, so the emission rate due to these protons could be reduced by a factor reaching ~2. For electrons, only a few percent of the SEP electrons can reach the atmosphere due to the magnetic mirror effect (Jolitz et al., 2021), which might be applicable to low-energy protons.

6. Conclusions

Previous studies were not able to reproduce the observed SEP-induced CO_2^+ UVD auroral emission profiles with precipitating energetic electrons considering the electron energy flux during SEP events observed by MAVEN (Schneider et al., 2015; Gérard et al., 2017; Haider and Masoom, 2019). This study aimed to reproduce the observed CO_2^+ UVD profiles by taking into account the contribution of energetic protons reaching MeV energies. We developed a Monte Carlo model, PTRIP, which solves the transport of electrons, protons and hydrogen atoms through the Martian atmosphere. PTRIP is used

to investigate the contribution of electron- and proton-induced CO_2^+ UVD emissions by using the electron and proton fluxes observed by MAVEN. The PTRIP model was validated by comparing our results with previous models (Kallio and Barabash, 2001; Leblanc et al., 2002; Jolitz et al., 2017; Gérard et al., 2017; Haider and Masoom, 2019). Our results showed that proton-induced CO_2^+ UVD emission profiles are brighter, narrower in altitude, and have a lower peak altitude than electron-induced CO_2^+ UVD emission profiles. The sum of the electron- and proton-induced CO_2^+ UVD emission profiles displays similar shapes and altitude peaks as those of the observed profiles (Schneider et al. 2015; Schneider et al. 2018), and extension of energy up to 500 keV for electrons and 20 MeV for protons enabled us to obtain the emission profiles that are more similar to the observations. However, the calculated intensity is larger than the observed intensity by a factor of 2 during the December 2014 SEP event, a discrepancy that might be explained by SEP shadowing (Lillis et al., 2016), calculation geometry effect, and magnetic mirror effect (Jolitz et al., 2021). Therefore, the contribution of energetic protons help to reconcile the in situ observations of the SEP electrons and proton fluxes onboard MAVEN with the observed emission brightness observed by MAVEN/IUVS (Schneider et al., 2015, 2018) during the two SEP events. This conclusion should be confirmed by considering other SEP events and completed by taking into account other possible effects that can impact the reconstructed emission brightness profiles. However, it also invites more accurate investigations of the other possible effects of an SEP event in Mars' atmosphere, such as atmospheric heating or induced low altitude chemistry.

Acknowledgements

The modeling data supporting the figures presented in this paper are available at https://doi.org/10.5281/zenodo.5651712. This work was supported by JSPS KAKENHI Grant Number JP18H05439, JP18KK0093, JP19H00707, 19K03943, JP20H00192, and JP20H04605, and NINS Astrobiology Center satellite research. Y. Nakamura is supported by the International Joint Graduate Program in Earth and Environmental Sciences, Tohoku University (GP-EES). FL acknowledges the support by the ANR HELIOSARES (ANR-09- BLAN-0223), ANR MARMITE-CNRS (ANR-13-BS05-0012-02) and by the "Systéme Solaire" program of the French Space Agency CNES. Y. Nakamura would like to acknowledge J. Halekas, T. Hara, R. D. Jolitz, X. Shaosui, and N. M. Schneider for their help in processing the particle flux data observed by MAVEN/SEP and SWEA.

Reference

Basu, B., Jasperse, J. R., Robinson, R. M., Vondrak, R. R., and Evans, D. S. (1987). Linear transport theory of auroral proton precipitation: A comparison with observations, *J. Geophys. Res*., 92, 5920-5932, doi:10.1029/JA092iA06p05920.

Bertaux, J. L., Leblanc, F., Witasse, O., Quemerais, E., Lilensten, J., Stern, S. A., & Korablev, O. (2005). Discovery of an aurora on Mars, *Nature*, 435, 790-794, doi:10.1038/nature03603.

Bhardwaj, A., and Jain, S. K. (2009). Monte Carlo model of electron energy degradation in a CO_2 atmosphere, *J. Geophys. Res.*, 114, A11309, doi:10.1029/2009JA014298.

Bhardwaj, A., and Jain, S. K. (2013). CO Cameron band and CO_2^+ UV doublet emission in the dayglow of Venus: Role of CO in the Cameron band production, *J. Geophys. Res.: Space Physics*, 118, 3660-3671, doi:10.1002/jgra.50345.

Bisikalo, D. V., Shematovich, V. I., Gérard, J. -C., Hubert, B. (2017). Influence of crustal magnetic field on the Mars aurora electron flux and UV brightness, Icarus, 282, 127-135, doi:10.1016/j.icarus.2016.08.035.

Brain, D. A., Halekas, J. S., Peticolas, L. M., Lin, R. P., Luhmann, J. G., Mitchell, D. L., et al. (2006). On the origin of aurorae on Mars, *Geophys. Res. Lett*., 33, L01201, doi:10.1029/2005GL024782.

Deighan, J., Jain, S. K., Chaffin, M. S., Fang, X., Halekas, J. S., Clarke, J. T., et al. (2018). Discovery of proton aurora at Mars, *Nature Astronomy*, 2(10), 802-807, doi:10.1038/s41550-018-0538-5.

Ehresmann, B., Hassler, D. M., Zeitlin, C., Guo, J., Wimmer-Schweingruber, R. F., Matthiä, D., et al. (2018). Energetic particle radiation environment observed by RAD on the surface of Mars during the September 2017 event, *Geophys. Res. Lett*., 45, 5305-5311, doi:10.1029/2018GL077801.

Fang, X., Lummerzheim, D., and Jackman, C. H. (2013). Proton impact ionization and a fast calculation method, *J. Geophys. Res.: Space Physics*, 118, 5369-5378, doi:10.1002/jgra.50484.

878
879 Forget, F., Montmessin, F., Bertaux, J. - L., González - Galindo, F., Lebonnois, S.,
880 Quémerais, E., Reberac, A., Dimarells, E., and López - Valverde, M. A. (2009). Density
881 and temperatures of the upper Martian atmosphere measured by stellar occultations with
882 Mars Express SPICAM, J. Geophys. Res., 114, E01004, doi:10.1029/2008JE003086.
883
884 Fox, J. L., and Dalgarno, A. (1979). Ionization, luminosity, and heating of the upper
885 atmosphere of Mars, *J. Geophys. Res*., 84, 7315-7333, doi:10.1029/JA084jA12p07315.
886
887 Gérard, J. -C., Soret, L., Shematovich, V. I., Bisikalo, D. V., and Bougher, S. W. (2017).
888 The Mars diffuse aurora: A model of ultraviolet and visible emissions, *Icarus*, 288, 284-
889 294, doi:10.1016/j.icarus.2017.01.037.
890
891 Green, A. E. S., and Sawada, T. (1972). Ionization cross sections and secondary electron
892 distributions, *Journal of Atmospheric and Terrestrial Physics*, 34, 10, 1719-1728,
893 doi:10.1016/0021-9169(72)90031-1.
894
895 Gröller, H., Montmessin, F., Yelle, R. V., Lefèvre, F., Forget, F., Schneider, N. M., et al.
896 (2018). MAVEN/IUVS stellar occultation measurements of Mars atmospheric structure
897 and composition, *J. Geophys. Res.: Planets*, 123, 1449-1483, doi:10.1029/2017JE005466.
898
899 Haider, S. A., Seth, S. P., Kallio, E., and Oyama, K. I. (2002). Solar EUV and electron-
900 proton-hydrogen atom-produced ionosphere on Mars: Comparative studies of particle
901 fluxes and ion production rates due to different processes, *Icarus*, 159(1), 18-30.
902 doi:10.1006/icar.2002.6919.
903
904 Haider, S. A., and Masoom, J. (2019). Modeling of Diffuse Aurora due to Precipitation
905 of H^+ - H and SEP Electrons in the Nighttime Atmosphere of Mars: Monte Carlo
906 Simulation and MAVEN Observation, *J. Geophys. Res.: Space Physics*, 124, 9566-9576,
907 doi:10.1029/2019JA026688.
908
909 Hassler, D. M., Zeitlin, C., Ehresmann, B., Wimmer-Schweingruber, R. F., Guo, J.,
910 Matthiä, D., et al (2018). Space weather on the surface of Mars: Impact of the September
911 2017 events, *Space Weather*, 16, 1702-1708, doi:10.1029/2018SW001959.
912
913 Hughes, A., Chaffin, M., Mierkiewicz, E., Deighan, J., Jain, S., Schneider, N., et al.

(2019). Proton aurora on Mars: A dayside phenomenon pervasive in southern summer, *J. Geophys. Res.: Space Physics*, 124, 10533-10548. doi:10.1029/2019JA027140.

Itikawa, Y. (2002). Cross sections for electron collisions with carbon dioxide, *J. Phys. Chem. Ref. Data*, 31, 749, doi:10.1063/1.1481879.

Itikawa, Y. (2006). Cross sections for electron collisions with nitrogen molecules, *J. Phys. Chem. Ref. Data*, 35, 31, doi:10.1063/1.1937426.

Itikawa, Y. (2009). Cross sections for electron collisions with oxygen molecules, *J. Phys. Chem. Ref. Data*, 38, 1, doi:10.1063/1.3025886.

Itikawa, Y. (2015). Cross sections for electron collisions with carbon monoxide, *J. Phys. Chem. Ref. Data*, 44, 013105, doi:10.1063/1.4913926.

Jackman, C. H., Garvey, R. H., and Green, A. E. S. (1977). Electron impact on atmospheric gases, I. Updated cross sections, *J. Geophys. Res.*, 82(32), 5081-5090, doi:10.1029/JA082i032p05081.

Jolitz, R. D., Dong, C. F., Lee, C. O., Lillis, R. J., Brain, D. A., Curry, S. M., et al. (2017). A Monte Carlo model of crustal field influences on solar energetic particle precipitation into the Martian atmosphere, *J. Geophys. Res.: Space Physics*, 122, 5653-5669, doi:10.1002/2016JA023781.

Jolitz, R. D., Dong, C. F., Rahmati, A., Brain, D. A., Lee, C. O., Lillis, R. J., et al. (2021). Test particle model predictions of SEP electron transport and precipitation at Mars, *J. Geophys. Res.: Space Physics*, 126, e2021JA029132, doi:10.1029/2021JA029132.

Kallio, E., and Barabash, S. (2001). Atmospheric effects of precipitating energetic hydrogen atoms on the Martian atmosphere, *J. Geophys. Res*., 106(A1), 165-177, doi:10.1029/2000JA002003.

Kozelov, B.V., and Ivanov, V.E. (1992). Monte Carlo calculation of proton-hydrogen atom transport in N_2, *Planetary and Space Science*, 40, 11, 1503-1511, doi:10.1016/0032-0633(92)90047-R.

Larson, D. E., Lillis, R. J., Lee, C. O., Dunn, P. A., Hatch, K., Robinson, M., et al. (2015). The MAVEN Solar Energetic Particle Investigation, *Space Sci. Rev.*, 195, 153-172, doi:10.1007/s11214-015-0218-z.

Leblanc, F., Luhmann, J. G., Johnson, R. E., and Chassefiere, E., (2002). Some expected impacts of a solar energetic particle event at Mars, *J. Geophys. Res*., 107(A5), doi:10.1029/2001JA900178.

Lebonnois, S., Quémerais, E., Montmessin, F., Lefèvre, F., Perrier, S., Bertaux, J.-L., and Forget, F. (2006), Vertical distribution of ozone on Mars as measured by SPICAM/Mars Express using stellar occultations, *J. Geophys. Res.*, 111, E09S05, doi:10.1029/2005JE002643.

Lillis, R. J., Fillingim, M. O., and Brain, D. A. (2011). Three-dimensional structure of the Martian nightside ionosphere: Predicted rates of impact ionization from Mars Global Surveyor magnetometer and electron reflectometer measurements of precipitating electrons, *J. Geophys. Res*., 116, A12317, doi:10.1029/2011JA016982.

Lillis, R. J., Lee, C. O., Larson, D., Luhmann, J. G., Halekas, J. S., Connerney, J. E. P., and Jakosky, B. M. (2016). Shadowing and anisotropy of solar energetic ions at Mars measured by MAVEN during the March 2015 solar storm, *J. Geophys. Res.: Space Physics*, 121, 2818-2829, doi:10.1002/2015JA022327.

Lingam, M., Dong, C., Fang, X., Jakosky, B., and Loeb, A. (2018). The Propitious Role of Solar Energetic Particles in the Origin of Life, *The Astrophysical Journal*, 853:10, doi:10.3847/1538-4357/aa9fef.

Luhmann, J. G., Zeitlin, C., Turner, R., Brain, D. A., Delory, G., Lyon, J. G., and Boynton, W. (2007). Solar energetic particles in near-Mars space, *J. Geophys. Re*s., 112, E10001, doi:10.1029/2006JE002886.

Millour, E., Forget, F., Spiga, A., Vals, M., Zakharov, V., Montabone, et al. (2018). The Mars climate database (version 5.3), *From Mars express to ExoMars Scientific Workshop*, Madrid, Spain: ESA-ESAC.

Mitchell, D. L., Mazelle, C., Sauvaud, J.-A., Thocaven, J.-J., Rouzaud, J., Fedorov, A., et

al. (2016). The MAVEN Solar Wind Electron Analyzer, *Space Sci. Rev*., 200, 495-528, doi:10.1007/s11214-015-0232-1.

Nigam, B. P. and Sundaresan, M. K. and Wu, T. -Y. (1959). Theory of Multiple Scattering: Second Born Approximation and Corrections to Molière's Work, *Phys. Rev*., 115, 3, 491-502, doi:10.1103/PhysRev.115.491.

Noël, S., and Prölss, G. W. (1993). Heating and radiation production by neutralized ring current particles, *J. Geophys. Res.*, 98(A10), 17317-17325, doi:10.1029/93JA01500.

Porter, H. S., and Jump, F. W. (1978). Analytical total angular elastic electron impact cross sections for planetary atmospheres, *NASA Publ.*, CSC/TM.

Porter, H. S., Varosi, F., and Mayr, H. G. (1987). Iterative solution of the multistream electron transport equation: 1. Comparison with laboratory beam injection experiments, *J. Geophys. Res*., 92(A6), 5933-5959, doi:10.1029/JA092iA06p05933.

Rieke, Foster F. and Prepejchal, W. (1972). Ionization Cross Sections of Gaseous Atoms and Molecules for High-Energy Electrons and Positrons, *Phys. Rev. A*, 6, 4, 1507-1519, doi:10.1103/PhysRevA.6.1507.

Ritter, B., Gérard, J.-C., Hubert, B., Rodriguez, L., and Montmessin, F. (2018). Observations of the proton aurora on Mars with SPICAM on board Mars Express, *Geophys. Res. Lett.*, 45, 612–619, doi:10.1002/ 2017GL076235.

Rudd, M. E., DuBois, R. D., Toburen, L. H., Ratcliffe, C. A., and Goffe, T. V. (1983). Cross sections for ionization of gases by 5-4000-keV protons and for electron capture by 5-150-keV protons, Phys. Rev. A, 28, 6, 3244-3257, doi:10.1103/PhysRevA.28.3244.

Schneider, N. M., Deighan, J. I., Jain, S. K., Stiepen, A., Stewart, A. I. F., Larson, D. et al. (2015). Discovery of diffuse aurora on Mars, *Science*, 350, 6261, doi:10.1126/science.aad0313.

Schneider, N. M., Jain, S. K., Deighan, J., Nasr, C. R., Brain, D. A., Larson, D., et al. (2018). Global aurora on Mars during the September 2017 space weather event, *Geophys. Res. Lett.*, 45, 7391-7398, doi:10.1029/2018GL077772.

Shute, G. G., Robson, D., McKenna, V. R., and Berztiss, A. T. (1962). Elastic scattering of protons by carbon, Nuclear Physics, 37, 535-553, doi:10.1016/0029-5582(62)90289-4.

Solomon, S. C. (2001). Auroral particle transport using Monte Carlo and hybrid methods, *J. Geophys. Res*., 106(A1), 107-116, doi:10.1029/2000JA002011.

Swartz, W. E., Nisbet, J. S., and Green, A. E. S. (1971). Analytic expression for the energy-transfer rate from photoelectrons to thermal-electrons, *J. Geophys. Res*., 76(34), 8425-8426, doi:10.1029/JA076i034p08425.

Vahedi, V., and Surrendra, M. (1995). A Monte Carlo collision model for the particle-in-cell method: applications to argon and oxygen discharges, Computer Physics Communications, 87, 1-2, 179-198, doi:10.1016/0010-4655(94)00171-W.

Yalcin, S., Gurler, O., Gultekin, A., and Gundogdu, O. (2006). An analytical expression for electron elastic scattering cross section from atoms and molecules in 1.0 keV to 1.0 MeV energy range, Phys. Lett. A, 356, 2, 138-145, doi:10.1016/j.physleta.2006.04.037.